



Original article

Advanced taper tension profile for improved control performance in roll-to-roll winding processes

Jaehyun Noh ^a, Minho Jo ^a, Minjae Kim ^a, Changwoo Lee ^{b,*}^a Department of Mechanical Design and Production Engineering, Konkuk University, 120 Neungdong-ro, Gwangjin-gu, Seoul 05029, South Korea^b Department of Mechanical Engineering, Konkuk University, 120 Neungdong-ro, Gwangjin-gu, Seoul 05029, South Korea

ARTICLE INFO

Keywords:
 radial stress
 roll-to-roll
 taper tension control
 winding process
 wound roll defects

ABSTRACT

Products coated with flexible film can be stored in wound rolls after the winding process. However, if the roll product experiences excessive internal stress, it can lead to various defects in the coated layer. To alleviate the stress within the wound roll, a taper tension profile is utilized to progressively reduce tension as the winding length increases. As a substantial amount of web is wound onto the core, the moment of inertia of the wound roll increases. It has been observed that, as the winding length increases, the tension control performance of the taper tension tends to deteriorate. We propose an advanced taper tension profile to enhance tension control performance and validates the effectiveness of this profile through winding experiments. It was observed that, compared to the parabolic taper tension, maximum tension error could be reduced by approximately 16.1% throughout the winding process. This reduction in tension error enables the preservation of the radial stress reduction effect of the taper tension, resulting in a 13.3% decrease in the maximum radial stress compared to the parabolic taper tension. The proposed taper tension profile contributes to a more uniform quality of the coated layer, especially as the maximum winding length is extended.

1. Introduction

Roll-to-roll manufacturing systems have traditionally found application in the production of solid oxide fuel cell (SOFC) electrolytes [1,2], solar cells [3,4], organic light-emitting diodes [5,6], thin-film transistors (TFTs) [7,8], among others. These systems excel in coating, printing, and drying processes while consistently moving a web at high speeds. Recently, there has been a sharp rise in the demand for batteries due to the electrification of the automotive industry, leading to the increased utilization of roll-to-roll manufacturing systems in various industries [9, 10]. To meet this growing demand, this technology allows for the mass production of battery electrodes over large areas.

A roll-to-roll system typically consists of an unwinder, infeeder, outfeeder, and rewinder, all driven by motors [11]. The section between the driven rolls is known as a span, and the tension on the web varies within each span. The unwinding section supplies raw materials such as PET film, copper foil, and aluminum foil [12,13]. The section between the infeeder and outfeeder is where processes such as slot-die coating and printing take place [14,15]. Following these processes, the web is

transported to a lengthy drying system to dry the applied solution [16, 17]. After drying, the web and coated layer are wound onto rolls around a central core in the rewinder section, facilitating efficient storage in a compact state [18,19].

Defects in products produced by roll-to-roll systems frequently occur during drying and winding process [20,21,22,23]. Wrinkle defects can arise when the moving web experiences an uneven temperature distribution within the dryer [24]. These temperature variations can result in strain deviations in both the machine direction (MD) and cross-machine direction (CMD), thus ultimately causing wrinkles in the web. Consequently, guidelines for optimizing process conditions to reduce web wrinkle defects within the dryer were introduced.

Jeon et al. identified tension reduction caused by thermal deformation in the web while passing through the dryer and proposed a novel feed-forward tension control logic to counteract this phenomenon [25]. By accurately forecasting the temperature distribution of the web within the dryer using the finite element method and predicting the speed adjustment needed for the driven rolls based on this temperature prediction, a consistent tension was maintained as the web entered the dryer.

Abbreviations: CMD, cross-machine direction; EPC, edge position controller; FSR, force sensing resistor; GDC, gadolinium-doped ceria; MD, machine direction; MSD, master speed drive; PLC, programmable logic controller; SEM, scanning electron microscopy.

* Corresponding author.

E-mail address: leewoo1220@konkuk.ac.kr (C. Lee).

<https://doi.org/10.1016/j.aej.2024.06.068>

Received 8 November 2023; Received in revised form 21 May 2024; Accepted 23 June 2024

Available online 28 June 2024

1110-0168/© 2024 The Author(s). Published by Elsevier BV on behalf of Faculty of Engineering, Alexandria University This is an open access article under the CC BY-NC-ND license (<http://creativecommons.org/licenses/by-nc-nd/4.0/>).

Additionally, in industries that use roll-to-roll technology, a larger amount of coated or printed layers are wound onto a single central core to enhance productivity [26,27,28]. This practice subjects the web to circumferential and radial stresses, which can lead to unintended defects [29,30,31,32]. Noh et al. identified coated layer defects resulting from excessive radial stress when storing large quantities of coated layers in rolls after winding process [33]. They proposed a taper tension profile to mitigate these defects as the storage time increased.

To address these potential defects, several researchers have attempted to predict internal stress in wound rolls, developing various mathematical models. Altmann initially derived a general solution for the properties of linear elastic roll material using nonlinear constitutive relations to determine radial and hoop stress within linear elastic roll materials [34]. Yagoda then provided an explicit closed-form analytical solution for radial and hoop stress, predicting internal stress [35]. Additionally, the study predicted the behavior of internal stresses around the core of the wound roll and provided instructions to prevent core design and starting defects. Unlike previous studies, Hakiel introduced nonlinear material properties and applied the finite difference technique to establish a nonlinear stress model for center-wound roll, including a variable radial-direction modulus based on interlayer pressure [36]. Good et al. compared predicted stresses using Hakiel's model with measured values and identified a two-fold overprediction, incorporating a new term to account for nip-induced tension in the wound roll [37].

Burns et al. proposed strain-based formulas for stresses in profiled center-wound rolls by modeling residual stresses [38]. Their approach suggests that residual strains generate radial and hoop stress within the roll, and their novel system modeled the center-wound roll based on the residual strains. This model, however, is limited in its application to materials with low density and bending stiffness. Lee et al. addressed this limitation by developing an advanced stress model that considers the density and bending stiffness of the web, resulting in more accurate predictions of internal stress [39].

Excessive stress inside the wound roll can lead to degraded quality uniformity of the final product. The most effective way to prevent this defect is to apply a taper tension profile. However, as the length of the web wound on a single core increases to improve productivity, the moment of inertia of the rewinder increases. The increased moment of inertia of the rewinder is a major cause of tension error when using a taper tension profile. In this study, a new polynomial-based taper tension profile is developed to effectively reduce the radial stress and minimize the defects of the coated layer in a production process where the winding length gradually increases, and the radial stress mitigation effect is analyzed by conducting a roll-to-roll winding process.

2. Mathematical model of wound roll stress

Fig. 1(a) illustrates a schematic of a wound roll within a roll-to-roll winding process. The critical factor influencing the stress within the wound roll during its formation is the winding tension [40,41]. The components within the wound roll are detailed in **Fig. 1(b)**, which are subject to radial and circumferential stresses. Burns et al. developed a

novel mathematical model to represent the stresses inside the wound roll based on a force balance equation [38]. **Table 1** defines the meaning of symbols used in the mathematical model. Burns' model led to the derivation of a new relationship between hoop stress in the circumferential direction, radial stress in the radial direction, and the definition of residual stress. **Eq. (1)** defines the total strain in the radial direction, while **Eq. (2)** defines the total strain in the hoop direction. The interaction between the radial and hoop strains can be derived from the following two equations, as shown in **Eq. (3)**.

$$\varepsilon_{rr,\text{total}} = \varepsilon_{rr} + \varepsilon_{rr}^* = \frac{du}{dr} \quad (1)$$

$$\varepsilon_{\theta\theta,\text{total}} = \varepsilon_{\theta\theta} + \varepsilon_{\theta\theta}^* = \frac{ud\theta}{rd\theta} = \frac{u}{r} \quad (2)$$

$$r \frac{d\varepsilon_{\theta\theta}}{dr} + \varepsilon_{\theta\theta} - \varepsilon_{rr} = \varepsilon_{rr}^* - \varepsilon_{\theta\theta}^* - r \frac{d\varepsilon_{\theta\theta}^*}{dr} \quad (3)$$

For the wound roll element represented in **Fig. 1(b)**, the force balance equation can be expressed as follows:

$$\sigma_{rr} + r \frac{d\sigma_{rr}}{dr} - \sigma_{\theta\theta} = 0 \quad (4)$$

Letting the operator be $D = r \frac{d}{dr}$, **Eq. (4)** can be expressed as follows.

$$(1+D)\sigma_{rr} = \sigma_{\theta\theta} \quad (5)$$

Under the assumption that strain and stress exhibit a linear relationship in Burns' model, inserting **Eq. (5)** into the generalized Hooke's

Table 1
Definitions of symbols.

Symbols	Meaning
ε_{rr}	Elastic strain in radial direction
ε_{rr}^*	Residual strain in radial direction
$\varepsilon_{\theta\theta}$	Elastic strain in circumferential direction
$\varepsilon_{\theta\theta}^*$	Residual strain in circumferential direction
u	Radial displacement
r	Radius ratio
σ_{rr}	Radial stress
$\sigma_{\theta\theta}$	Hoop stress
σ^*	Residual stress
s_{ij}	Elastic compliance
i, j	Direction of compliance (1: Radial, 2: Circumferential, 3: Width)
σ_w	Winding stress
ν	Poisson's ratio
R	Maximum radius ratio
E_c	Elastic modulus of core
σ_0	Initial winding stress
T_{constant}	Constant winding tension
T_{linear}	Linear taper tension
$T_{\text{parabolic}}$	Parabolic taper tension
T_{poly}	Poly taper tension
T_0	Initial winding tension
taper	Taper value
n	Order of the poly taper tension

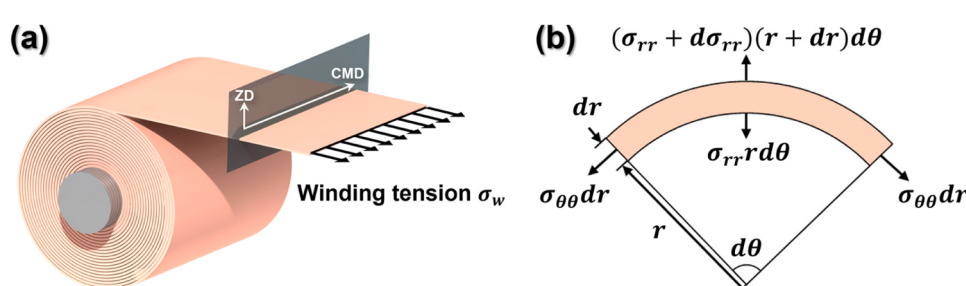


Fig. 1. (a) Schematic of a wound roll manufactured using a roll-to-roll winding system, (b) forces acting on an element inside a wound roll.

law and its application to Eq. (3) yields a second-order differential equation, as depicted in Eq. (6).

$$\{D^2 + 2D + (1 - \beta^2)\} \sigma_{rr} = \sigma^* \quad (6)$$

where

$$\beta^2 = \frac{s_{11}s_{33} - s_{13}^2}{s_{22}s_{33} - s_{23}^2} = \frac{s_{11}}{s_{22}} \quad (7)$$

and the residual stress σ^* is

$$\sigma^* = \frac{d}{dr}(r\sigma_w) + \nu\sigma_w \quad (8)$$

Solving the second-order differential equation in Eq. (6), the radial stress can be derived as follows:

$$\sigma_{rr}(r) = \frac{1}{r} \left[B \left(r^\beta - \frac{R^{2\beta}}{r^\beta} \right) + \frac{1}{2\beta} \left\{ r^{-\beta} \int_r^R t^\beta \sigma^*(t) dt - r^\beta \int_r^R t^{-\beta} \sigma^*(t) dt \right\} \right] \quad (9)$$

where

$$B = \frac{2\beta\sigma_0 E_c s_{22} - \left[\{E_c(s_{12} - \beta s_{22}) - 1\} \int_1^R t^\beta \sigma^*(t) dt \right] + \left[\{1 - E_c(s_{12} + \beta s_{22})\} \int_1^R t^{-\beta} \sigma^*(t) dt \right]}{2\beta \{(s_{12}E_c - 1)(1 - R^{2\beta}) + \beta E_c s_{22}(1 + R^{2\beta})\}} \quad (10)$$

3. Taper tension control in roll-to-roll winding systems

The roll-to-roll manufacturing system used in this study, installed at Konkuk University, Seoul, South Korea, is depicted in Fig. 2(a-d). Tension control is implemented in both the unwinding and rewinding span through a feedback loop based on a dancer system. The master speed drive (MSD), which operates at the speed set, is designated as the infeed

roll [42,43]. The unwinding span responsible for feeding the web is shown in Fig. 2(b). After coating and printing, the web is conveyed to the drying system, as shown in Fig. 2(c). Finally, the rewinding span is responsible for winding the dried coated layer or printed pattern, as depicted in Fig. 2(d).

During the roll-to-roll winding process, it is widely recognized that the most effective method to mitigate defects occurring within the wound roll is to implement an appropriate taper tension profile [44]. Taper tension involves gradually reducing tension relative to the initial set tension as the winding length increases. In general, the taper value represents the ratio of the reduced tension to the initial set tension.

Various taper tension profiles have been studied with an aim to reduce the tension when executing the winding process. These include the linear taper tension profile, which maintains a constant slope for tension reduction, and the parabolic taper tension profile, which involves a significant reduction in tension at the outset of the winding process [39]. The linear taper tension profile is frequently employed in various roll-to-roll system-based industrial applications due to its consistent tension change rate and ease of application. The parabolic taper tension profile determines the shape of the taper tension profile by considering the maximum radius ratio and taper value and is recognized for its effectiveness in reducing radial stress by substantially decreasing

tension at the start of the winding process.

Within a roll-to-roll manufacturing system, tension plays a pivotal role as a process variable; furthermore, it is imperative to maintain tight control over the tension applied to the web and ensure that it closely aligns with the user-set tension value [45,46]. Typically, in roll-to-roll facilities, a feedback system employing a dancer or load cell is employed for tension control [47,48]. The utilization of the dancer

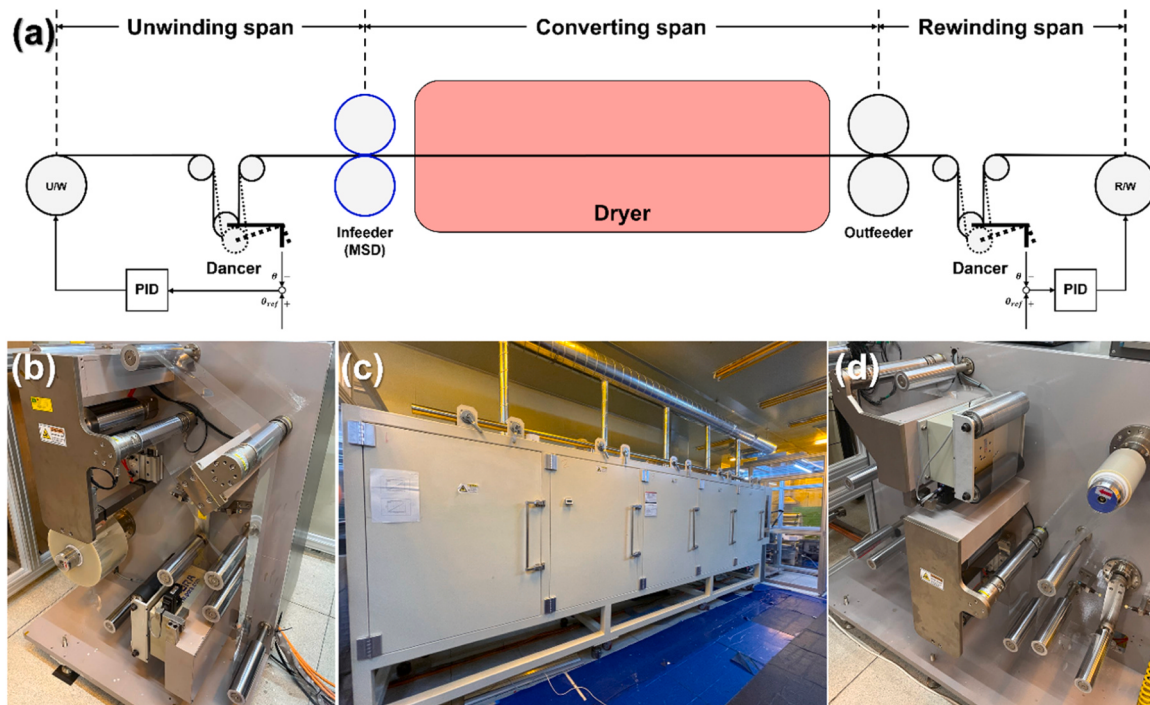


Fig. 2. (a) Roll-to-roll manufacturing system schematic, (b) unwinding span, (c) dryer system, (d) rewinding span.

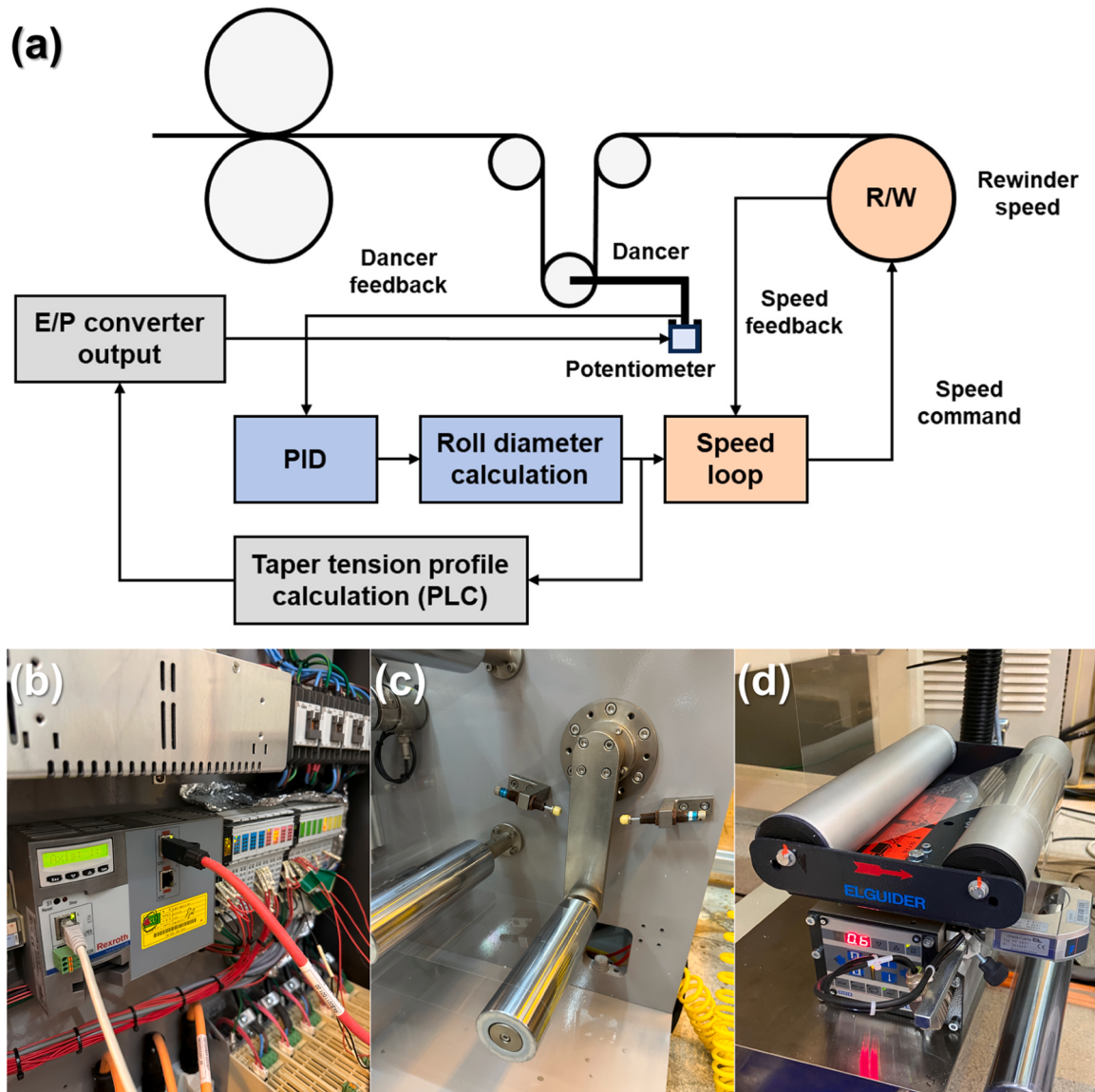


Fig. 3. (a) Dancer system-based tension control on a rewinding span, (b) programmable logic controller (PLC), (c) dancer system, (d) edge position controller (EPC).

feedback control method within this system is advantageous in mitigating tension disturbances. The taper tension control method using the dancer system is illustrated in Fig. 3(a). The position of the dancer is measured by a potentiometer, and this measurement is utilized as a feedback signal. The user-defined taper tension profile is calculated by the programmable logic controller (PLC), as demonstrated in Fig. 3(b), and is implemented by adjusting the air pressure in the dancer's pneumatic cylinder. Furthermore, to consistently maintain the dancer roll's position, as shown in Fig. 3(c), the PID controller computes and applies the rewind roll's speed command, utilizing data from the position of the dancer, center core radius, and current radius of the wound roll. The ratio between the current radius of the wound roll and the center core radius is expressed as the radius ratio.

When applying a taper tension profile, sudden changes in tension may cause the web to slip on the roll, resulting in lateral displacement [49,50]. This, in turn, can lead to telescoping defects in the wound roll. To mitigate this issue, an edge position controller (EPC), illustrated in Fig. 3(d), is utilized to maintain the lateral position of the web, thus minimizing the telescoping defect. In this study, various winding tension profiles, including constant, linear, and parabolic forms, were applied to analyze radial stress distribution. Additionally, a newly proposed poly

taper tension profile was included for examination. The different profiles are expressed as follows.

$$T_{\text{constant}}(r) = T_0 \quad (11)$$

$$T_{\text{linear}}(r) = T_0 \left[1 - \left(\frac{\text{taper}}{100} \right) \cdot \left(\frac{r-1}{R-1} \right) \right] \quad (12)$$

$$T_{\text{parabolic}}(r) = T_0 \left[1 - \left(\frac{\text{taper}}{100} \right) \cdot \frac{\sqrt{(r-1)(2R-r-1)}}{(R-1)} \right] \quad (13)$$

$$T_{\text{poly}}(r) = T_0 \left[1 - \left(\frac{\text{taper}}{100} \right) \cdot \left(\frac{r-1}{R-1} \right)^n \right] \quad (14)$$

To measure the tension in the rewinding span during the winding process, a load cell, illustrated in Fig. 4(a), was affixed to the idle roll. A tension data acquisition unit, displayed in Fig. 4(b), was utilized to record the real-time tension measurements provided by the load cell. The slot-die coating system, depicted in Fig. 5(a), was utilized to create the coated layer. As shown in Fig. 5(b), the gadolinium-doped ceria (GDC, Sigma Aldrich, St. Louis, MO, USA) coating layer used for SOFC electrolytes was applied to PET film (CD901, KOLON Inc., Seoul, South Korea).

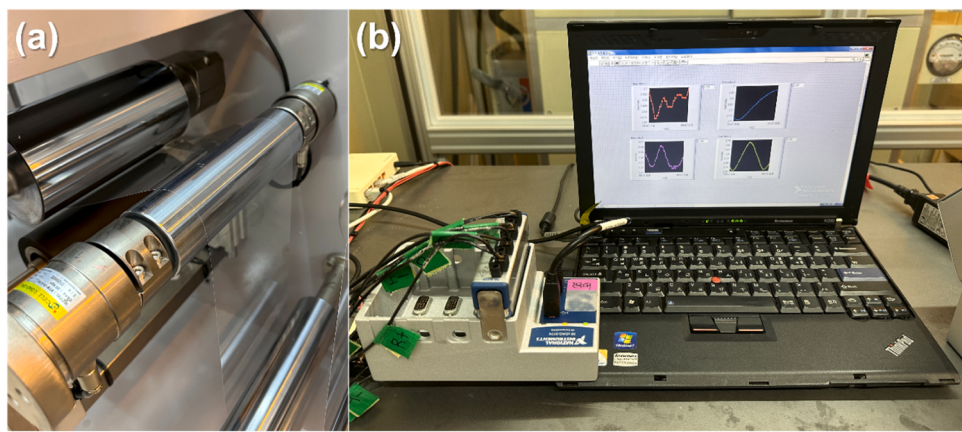


Fig. 4. (a) Load cell for measuring tension in a rewinding span, (b) real-time tension data acquisition system configuration.

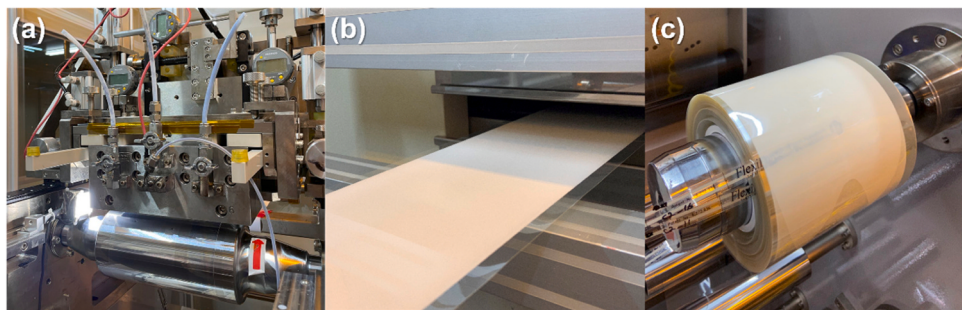


Fig. 5. (a) Roll-to-roll slot-die coating unit, (b) gadolinium-doped ceria (GDC) coating layer, (c) wound roll with force sensing resistors (FSRs) attached during the winding process.

To assess radial stress, a force sensing resistor (FSR, Tekscan Inc., Boston, MA, USA) was attached to each designated measurement point, as illustrated in Fig. 5(c). As the winding length increases, the mass of the web wound onto the rewind roll grows in comparison to the beginning of the winding process. Consequently, the moment of inertia of the wound roll also increases. Compared to the preset taper tension profile, a rewind roll with an increased moment of inertia exhibits a slower response to the speed command, resulting in an increased tension error. This increased tension error diminishes the effectiveness of the specified taper tension profile. Therefore, this study introduced a novel taper tension profile designed to maintain the profile's efficacy in production processes requiring further increases in winding length.

Table 2 presents the operating conditions within the rewinding section. The maximum operating tension in a roll-to-roll system should be set to a value corresponding to 6.67 % of the yield strength of the web [51]. We conducted a tensile test on PET film according to ASTM D882 and obtained a yield strength of 110 MPa at room temperature. The operating tension corresponding to within 6.67 % of the yield strength was determined. This precaution is taken to avoid plastic deformation, which may occur if the web is subjected to stress beyond its yield strength, particularly when encountering various tension disturbances.

These disturbances can manifest when the system is accelerated from an initial stop or when it is brought to a halt after being in motion. The constant, linear, and parabolic winding tension profiles can be expressed as mathematical models and are reported to be widely used in actual roll-to-roll winding processes [39]. We aimed to verify the effects of existing winding tension profiles and compare them with the poly taper tension profile. Additionally, as the taper value increases, the maximum radial stress reduction effect also increases. However, the rate of decrement in the taper tension profile also increases with higher taper values, which raises the likelihood of a telescoping defect. The value of telescoping is greatly influenced not by the magnitude of the taper tension but by the rate of its decrement [39]. The measuring range of the edge position sensor used during the winding process is ± 3 mm. If more than 30 % of the taper tension profile is applied, the EPC cannot control the telescoping defect within this range. Therefore, a 30 % taper value was applied, as it can significantly reduce radial stress while minimizing telescoping. Wound rolls are produced with a maximum radius ratio of 2.77 for 400 m and a maximum radius ratio of 4.94 for 1400 m. To compare the effect of the moment of inertia based on the winding length, the winding process is conducted with a length difference of approximately 3.5 times. The operating speed and drying temperature were

Table 2
Operating conditions for roll-to-roll slot-die coating and winding process.

Conditions	Units	Case 1	Case 2	Case 3	Case 4	Case 5	Case 6	Case 7
Operating tension	N	49	49	49	49	49	49	49
Winding tension profile	-	Constant	Linear	Parabolic	Constant	Linear	Parabolic	Poly
Taper value	%	-	30	30	-	30	30	30
Maximum radius ratio	-	2.77	2.77	2.77	4.94	4.94	4.94	4.94
Operating speed	m/min	4.0	4.0	4.0	4.0	4.0	4.0	4.0
Coating gap	mm	0.1	0.1	0.1	0.1	0.1	0.1	0.1
Drying temperature	°C	55	55	55	55	55	55	55

Table 3

Properties of the film, core, and coating ink.

Property	Units	Value
Film	Type	- Polyethylene terephthalate (PET)
	Width	mm 150
	Thickness	mm 0.1
	Density	kg/m ³ 1390
	Elastic modulus (25 °C)	MPa 2530
	Poisson's ratio (25 °C)	- 0.3
	Yield strength (25 °C)	MPa 110
	Type	- Polypropylene
	Diameter	mm 87.2
	Width	mm 150
Core	Elastic modulus	MPa 1600
	Solute	- Gadolinium-doped ceria (GDC)
	Particle size	µm < 0.5
	Viscosity (25 °C)	cP 90
Coating ink	Solid contents	wt% 40
	Contact angle	° 34

selected within a range to ensure sufficient drying time and complete evaporation of all solvents, considering the length of the roll-to-roll dryer system. The coating gap was set within a range capable of forming a stable coating bead, considering the minimum permissible wet coating thickness range in the slot die coating process [52].

Table 3 indicates the dimensions and mechanical properties of the film and wound roll core used in the winding process. The elastic modulus and yield strength of the PET film were measured through tensile testing at room temperature, following the ASTM D882 standard. Additionally, the Poisson's ratio was calculated by measuring the deformation in both the length and width directions of the specimen. The elastic modulus of the core was measured through tensile tests using samples manufactured according to ASTM D638 standards. Table 3 also presents the characteristics of the coating ink used in the slot-die coating process. GDC is a material that can be used to fabricate the electrolyte layer of SOFCs. The coating ink adheres to the particle size specifications of the GDC powder. The viscosity of the GDC coating ink was measured using a viscometer (DV2T, Brookfield, Middleboro, MA, USA). The solid

content of the coating ink was calculated by dividing the measured dry sample weight by the total sample weight. The contact angle of the coating ink was measured using an analyzer (Phoenix 300, SEO, Suwon, South Korea) at room temperature.

Fig. 6(a-c) shows the tension data measured during the winding process of a 400 m web, illustrating the three distinct tension profiles: constant winding tension, maintaining a constant tension throughout; the linear taper tension profile, with a constant gradual decrease at a taper value of 30 %; and the parabolic taper tension profile, featuring a rapid decrease at the beginning of the process.

From the tension data, the tension error relative to the radius ratio was calculated. When applying constant winding tension, the effect of moment of inertia is relatively minor as the radius ratio increases since there is no change in the preset tension. The tension error was calculated by dividing the error between the reference winding tension profile and the measured tension data, which is represented by the dashed line at each radius ratio, by the operating tension of 49 N.

An equitable comparison of the errors between these profiles was achieved by applying both constant winding tension and taper tension. When constant winding tension is applied, the tension error remains within the range of ±5 % throughout the process. In contrast, in the case of linear and parabolic taper tension, the tension error marginally increases as the radius ratio of the wound roll rises, with a maximum tension error of approximately ±5.8 % and ±5.3 %, respectively, in the latter stages of the winding process. In the case of the parabolic taper tension profile, the tension undergoes substantial changes at the start when the radius ratio is small, resulting in a notable tension error initially compared to other profiles. As the winding process continues with a radius ratio of 2.0 or higher, the tension change rate of the parabolic taper tension profile decreases, and the linear taper tension profile displays the most significant tension error.

When the reference winding tension profile, depicted by the dotted line in Fig. 6(a-c), was applied, Burns' radial stress model was utilized to predict the radial stress generated at each location within the wound roll, as illustrated in Fig. 7(a). Subsequently, to estimate the radial stress reduction effect of applying taper tension, the difference between the radial stresses when applying constant winding tension and when applying linear and parabolic taper tension were determined, as

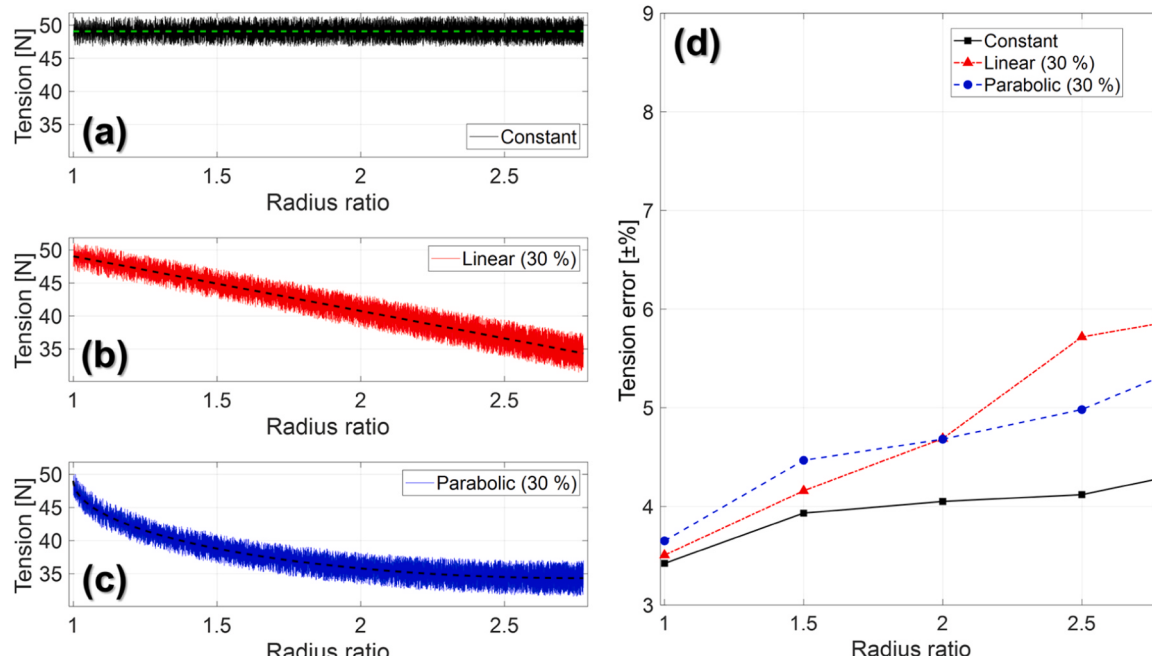


Fig. 6. Measured tension and tension error according to the winding tension with a maximum winding length of 400 m: (a) constant winding tension, (b) linear taper tension with 30 % of taper value, (c) parabolic taper tension with 30 % of taper value, (d) tension error depending on the radius ratio.

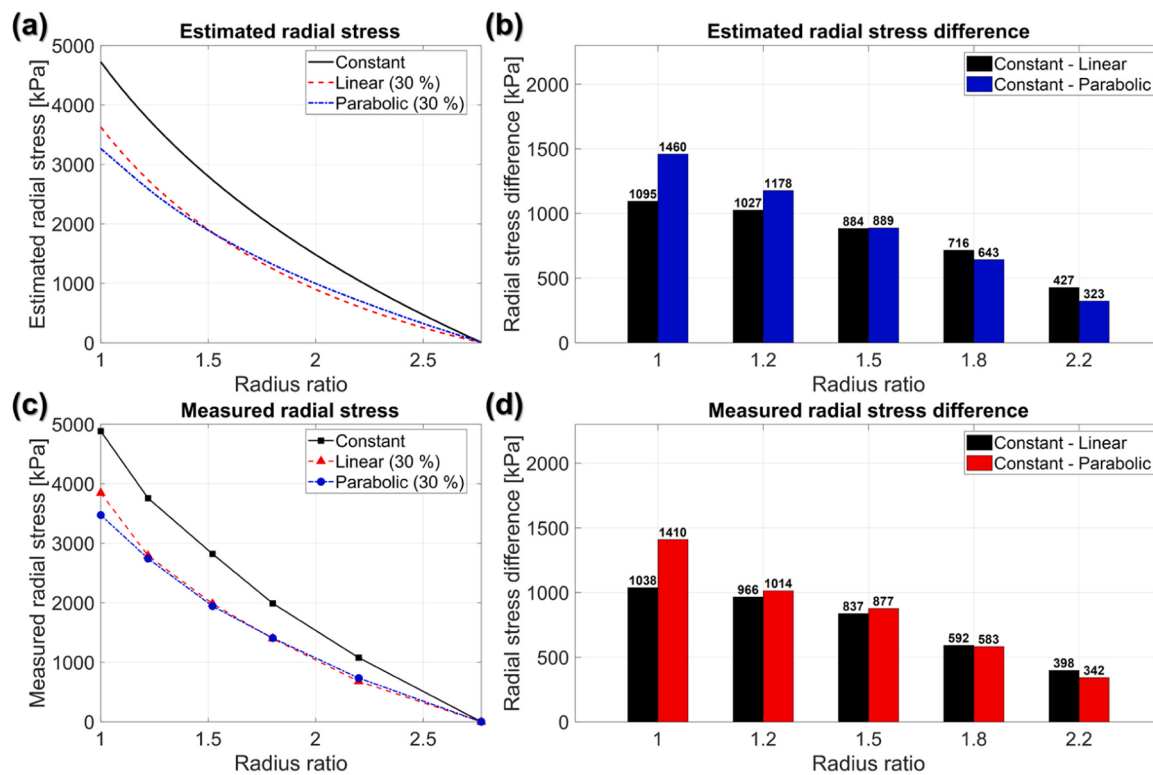


Fig. 7. (a) Estimated radial stress according to winding tension (constant, linear, parabolic) with a maximum winding length of 400 m, (b) reduction in estimated radial stress for taper tension profiles (linear, parabolic) compared to constant winding tension, (c) measured radial stress according to winding tension (constant, linear, parabolic) with a maximum winding length of 400 m, (d) reduction in measured radial stress for taper tension profiles (linear, parabolic) compared with constant winding tension.

displayed in Fig. 7(b). Furthermore, to evaluate the radial stress error due to the increase in winding length, the FSR from Fig. 5(c) was attached to positions with radius ratios of 1, 1.2, 1.5, 1.8, and 2.2 during the 400 m winding process. The measured radial stress values are shown in Fig. 7(c). The measured radial stress reduction achieved by linear and

parabolic taper tension compared to constant winding tension is illustrated in Fig. 7(d).

When the 400 m winding process was performed, the tension error was relatively small. Therefore, the errors between the predicted and measured radial stress values at the innermost layer for linear and

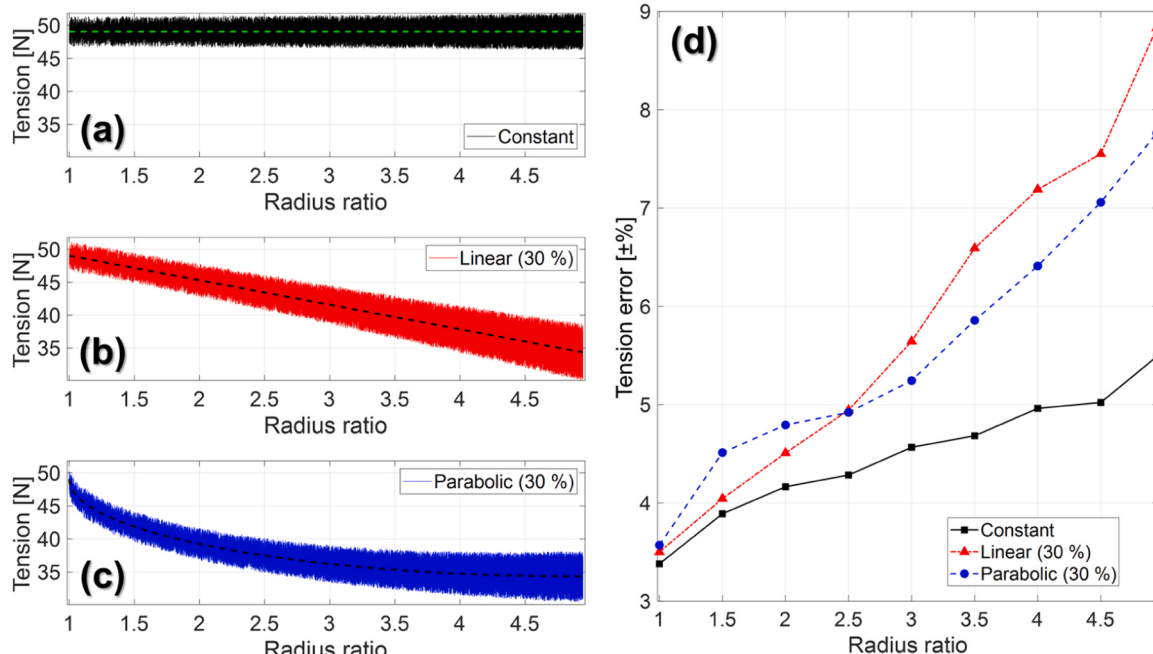


Fig. 8. Measured tension and tension error in accordance with winding tension with a maximum winding length of 1400 m: (a) constant winding tension, (b) linear taper tension with 30 % of taper value, (c) parabolic taper tension with 30 % of taper value, (d) tension error depending on the radius ratio.

parabolic taper tension were 5.2 % and 3.4 %, respectively. As a result, compared to constant winding tension, the radial stress reduction of linear and parabolic taper tension closely aligns with the prediction. Therefore, when the winding length is relatively short, the taper tension profile is closely followed since the change in the moment of inertia of the rewind roll is not significant. This ensures that the intended radial stress reduction effect is realized.

In the rewinding span, to maintain the dancer roll's position during the tension control process, the PID controller utilizes data from the dancer's position, center core radius, and current radius of the wound roll to calculate the speed command applied to the rewind roll. As the winding length continues to increase, the moment of inertia grows due to the accumulation of web on the rewind roll. This growth reduces the rewind roll's ability to precisely follow the calculated speed command, leading to an increase in tension error as the winding process advances, particularly when a greater maximum winding length of 1400 m is utilized.

Consequently, as presented in Fig. 8(a-c), the tension measurements can be observed to exhibit more significant disturbances compared to those shown in Fig. 6(a-c), where a maximum winding length of 400 m was employed. As displayed in Fig. 8(d), the effect of increasing the winding length is less pronounced in the case of constant winding tension, which features the lowest tension change rate based on the reference winding tension according to the radius ratio. On the other hand, linear and parabolic taper tensions involve relatively higher tension change rates, leading to a greater rate of tension error increase with extended winding lengths.

In the case of the parabolic taper tension, the tension error is substantial, particularly in the section with a small radius ratio, and beyond a radius ratio of approximately 2.5, the tension error increases as the tension change rate of the linear taper tension profile rises. Consequently, with the expansion of the maximum winding length, the radial stress reduction effect associated with the taper tension profiles can

substantially diminish.

Fig. 9(a) illustrates the predicted radial stress for a 1400 m winding process under a reference winding tension profile with no tension error. Fig. 9(b) shows the estimated radial stress reduction achieved with linear and parabolic taper tension profiles compared to constant winding tension. In an ideal scenario without tension error, the prediction indicates that the radial stress reduction effect is most pronounced when applying parabolic taper tension.

To measure the radial stress, FSR sensors were attached to points at the radius of 1.02, 1.20, 1.51, 1.82, 2.23, 2.71, 3.22, and 3.76. The results are displayed in Fig. 9(c), indicating an increase in radial stress values in both cases due to the increased tension error when applying the linear and parabolic taper tension profiles. Consequently, it can be observed in Fig. 9(d) that, compared to the constant winding tension, the radial stress reduction effect of both taper tension profiles is significantly reduced. The radial stress mitigating effect is found to be reduced by up to approximately 65.9 % for linear taper tension and up to approximately 50.3 % for parabolic taper tension. In other words, the intended effect of the taper tension profile cannot be accurately achieved if the tension control precision is reduced due to excessive winding length during the winding process.

4. Proposed taper tension profile

With the ongoing increase in winding length during the roll-to-roll winding process, the moment of inertia of the wound roll experiences a corresponding increase. Consequently, the tension error is most pronounced in the case of the linear taper tension profile, which maintains a relatively high tension change rate, even towards the end of the process. In contrast, the constant tension profile is the least affected by the moment of inertia of the wound roll because it sustains a consistent tension, resulting in the smallest tension error.

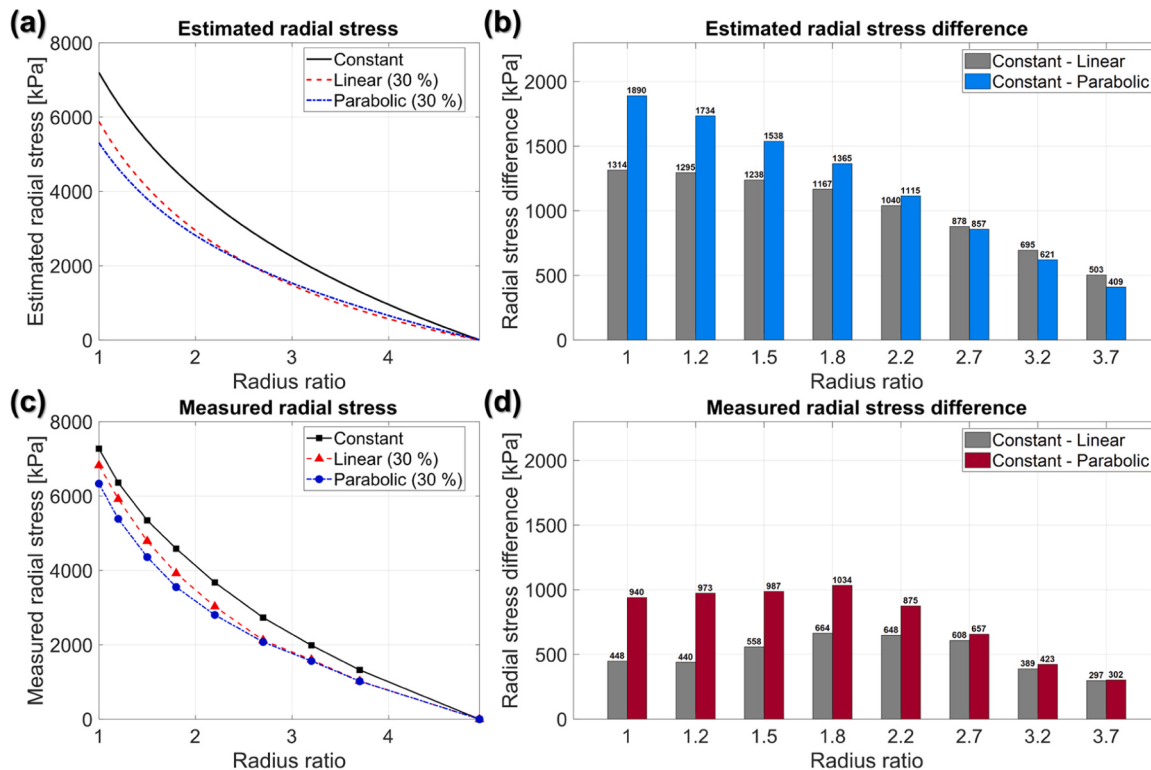


Fig. 9. (a) Estimated radial stress according to winding tension (constant, linear, parabolic) with a maximum winding length of 1400 m, (b) reduction in estimated radial stress for taper tension profiles (linear, parabolic) compared to constant winding tension, (c) measured radial stress according to winding tension (constant, linear, parabolic) with a maximum winding length of 1400 m, (d) reduction in measured radial stress for taper tension profiles (linear, parabolic) compared to constant winding tension.

In this study, recognizing that the parabolic taper tension profile exhibits a relatively low tension error due to its reduced tension change rate in the latter part of the winding process, a new polynomial-based taper tension profile, named poly taper tension, was developed to mitigate the impact of the moment of inertia. As the order of the polynomial increases, the tension diminishes sharply at the beginning of the winding process, and the rate of tension change decreases in subsequent phases, thus significantly mitigating the effect of the increased moment of inertia. By applying a poly taper tension profile, the performance degradation caused by the mounting tension error as the winding length increases can be minimized, achieving the desired reduction in radial stress.

The tension behavior of the parabolic taper tension is depicted in Fig. 10(a), while the tension behavior of the poly taper tension profile based on a 4th, 8th, 16th-order polynomial is presented in Fig. 10(b-d). To determine the order of the poly taper tension that exhibits reduced tension error compared to parabolic taper tension in long winding processes, the tension errors for different orders were compared. The winding process was performed using parabolic taper tension and poly taper tension with orders of $n = 4, 8$, and 16 . For the parabolic taper tension, the maximum tension error was 7.8% . In the case of the 4th order poly taper tension profile depicted in Fig. 10(b), the slope was relatively higher towards the end of the winding process, resulting in a tension error of 7.9% . When applying poly taper tension of order 8 or 16, after the rapid initial drop in tension, the rate of change in tension further decreases at a radius ratio of 1.15 . Consequently, when applying poly taper tension with higher orders, the tension error is initially larger than that of the parabolic profile. However, as the radius ratio increases, the tension error diminishes significantly compared to the parabolic profile, reaching approximately 6.5% and 6.3% , respectively, towards the end of the winding process. Thus, it is expected that as the order of the poly taper tension increases, the reduction effect on radial stress will be more significantly maintained.

However, rapid changes in tension during the winding process can cause lateral displacement of the web, a defect known as telescoping. The lateral displacement of the PET film was measured during the winding process using 8th and 16th order poly taper tension profiles.

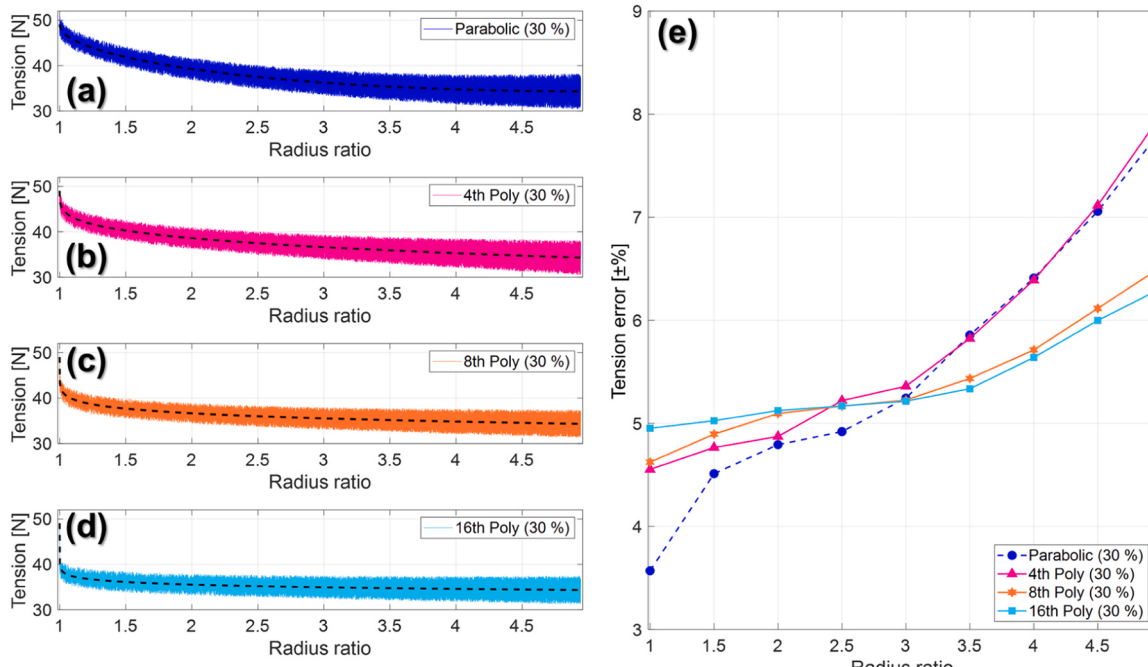


Fig. 10. Measured tension and tension error for parabolic and poly taper tension ($n=4, 8, 16$) with maximum winding length of 1400 m: (a) parabolic taper tension with 30 % of taper value, (b) poly taper tension ($n=4$) with 30 % of taper value, (c) poly taper tension ($n=8$) with 30 % of taper value, (d) poly taper tension ($n=16$) with 30 % of taper value, (e) tension error depending on the radius ratio.

Fig. 11(a) shows the lateral displacement when applying the 8th order poly taper tension profile, and Fig. 11(b) shows the lateral displacement when applying the 16th order profile. For the 8th order profile, which has a relatively lower rate of tension change at the beginning of the winding process, a maximum lateral displacement of 1.8 mm occurs, with telescoping observed up to a radius ratio of 1.16 . In contrast, when the 16th order profile is applied, the rate of tension change at the beginning is high, resulting in a lateral displacement beyond the measurement range of the edge position sensor, with telescoping observed up to a radius ratio of 1.19 . Consequently, considering the reduction effect on radial stress and telescoping defects, an 8th order poly taper tension profile was chosen.

Fig. 12(a) illustrates the predicted radial stress within the wound roll for when a winding tension profile with no tension error is applied. Based on the estimation, both the parabolic and poly taper tensions exhibit similar levels of radial stress. In Fig. 12(b), for the parabolic and poly taper tensions, the estimated radial stress is projected to decrease by approximately 1890 and 2170 kPa at a radius ratio of 1.02 , respectively, compared to the radial stress under constant winding tension. However, owing to the relatively larger winding tension error in the case of the parabolic taper tension from a radius of 2.98 onwards during the winding process, higher radial stresses are observed in Fig. 12(c) compared to the predicted values in Fig. 12(a). Meanwhile, the poly taper tension shows a relatively lower prediction error. Fig. 12(d) reveals that the radial stress reduction achieved with parabolic taper tension is approximately 940 kPa at a radius ratio of 1.02 , indicating a degradation in the radial stress reduction effect. Conversely, the poly taper tension profile results in a radial stress reduction of 1789 kPa , maintaining the intended radial stress reduction effect.

To verify the effect of radial stress on the quality of the coated layer within the wound roll, the coated layer thickness was measured using scanning electron microscopy (SEM, SU8010, Hitachi Inc., Tokyo, Japan), as depicted in Fig. 13(a). Fig. 13(b-d) display cross-sectional images of the coated layer around the center core with a radius of 1.02 , with a radius of 1.53 , and from the outer side with a radius of 4.93 , respectively. These images were obtained when applying the parabolic taper tension profile during a 1400 m winding process. In contrast,

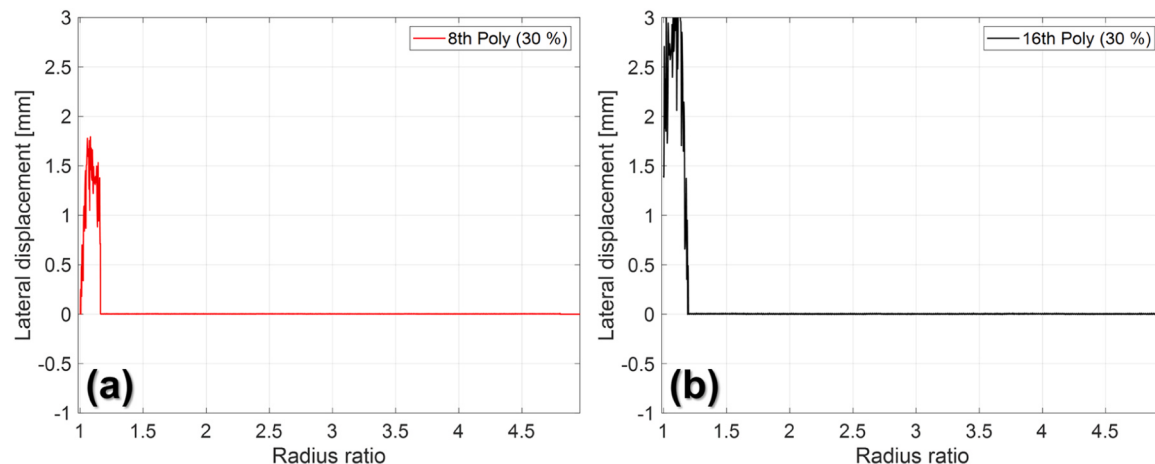


Fig. 11. (a) Lateral displacement of the web with the 8th order poly taper tension profile, (b) lateral displacement of the web with the 16th order poly taper tension profile.

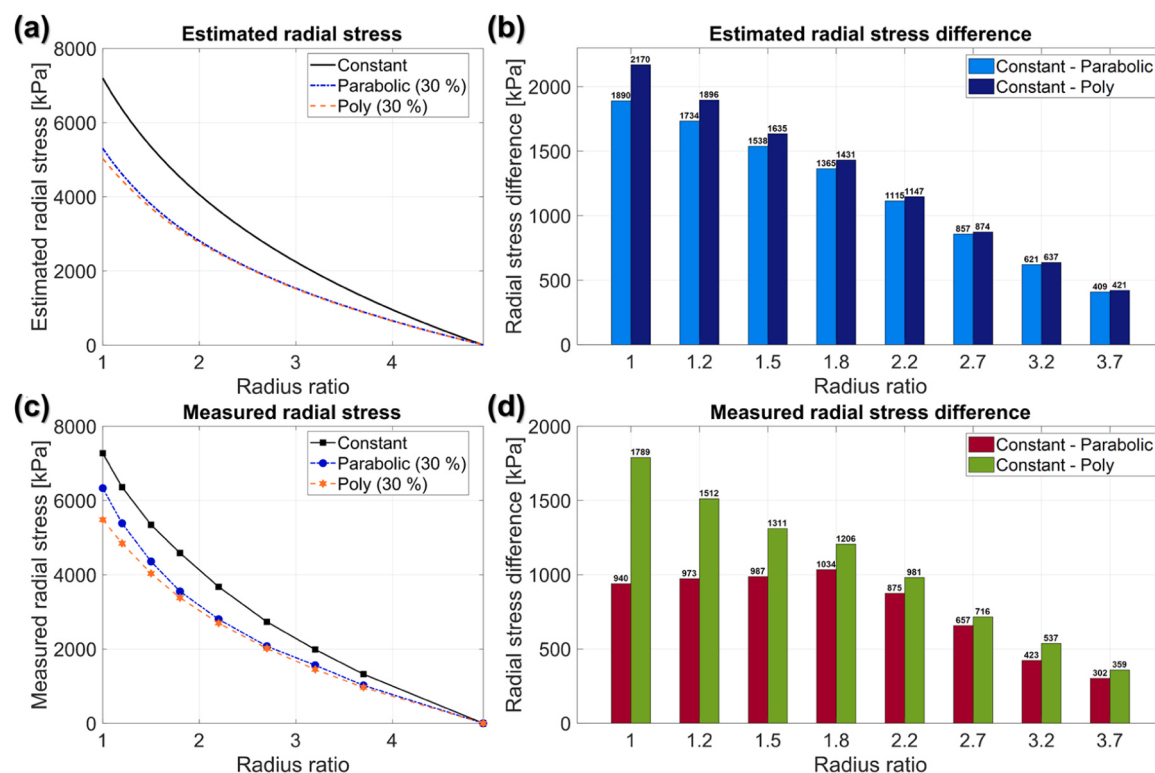


Fig. 12. (a) Estimated radial stress according to winding tension (parabolic, poly) with a maximum winding length of 1400 m, (b) reduction in estimated radial stress for taper tension profiles (parabolic, poly) compared to constant winding tension, (c) measured radial stress according to winding tension (parabolic, poly) with a maximum winding length of 1400 m, (d) reduction in measured radial stress for taper tension profiles (parabolic, poly) compared to constant winding tension.

Fig. 13(e-g) show cross-sectional images of the coated layer from the inner and outer sides of the wound roll when applying the poly taper tension profile.

As the winding length increases, the radial stress within the roll increases overall. The thickness of the coated layer on the inner side, where the radial stress is greatest, will be less than the thickness of the outer coated layer, where radial stress is minimal. The occurrence of this thickness reduction defect results in non-uniform coated layer thickness in the machine direction during subsequent stages. When the parabolic taper tension profile is applied, the radial stress reduction effect deteriorates due to tension errors arising from the increase in winding length. Consequently, compared to the thickness of the outer layer, the

thickness on the inner layer is reduced by 7.2 μm , as seen in Figs. 13(b) and 13(d).

In contrast, the poly taper tension profile effectively minimizes tension errors, even during a process with a relatively long winding length, thus preserving the radial stress reduction effect. Figs. 13(e) and 13(g) reveal a coated layer thickness reduction of 4.8 μm on the inner side, resulting in a 33.3 % improvement in the thickness uniformity of the coated layer compared to the parabolic taper tension profile.

The surface condition of the coated layer, which varies depending on the magnitude of radial stress, was observed with a microscope (Eclipse LV100ND, Nikon, Tokyo, Japan) in the vicinity of the samples, as shown in Figs. 13(b) and 13(e). During the 1400 m winding process with the

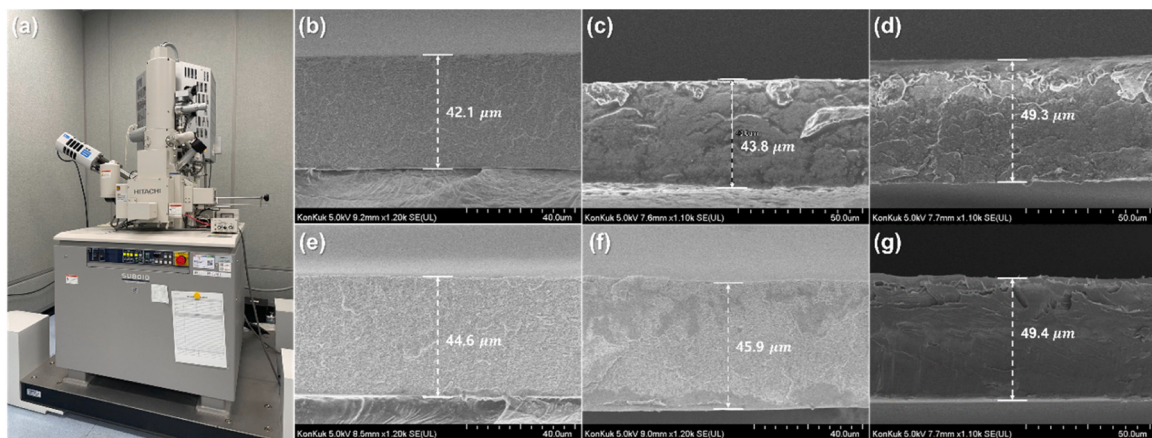


Fig. 13. (a) Scanning electron microscopy (SEM) instrument, (b) cross-sectional image of the coated layer at a radius ratio of 1.02 with a parabolic taper tension profile, (c) cross-sectional image of the coated layer at a radius ratio of 1.53 with a parabolic taper tension profile, (d) cross-sectional image of the coated layer at a radius ratio of 4.93 with a parabolic taper tension profile, (e) cross-sectional image of the coated layer at a radius ratio of 1.02 with a poly taper tension profile, (f) cross-sectional image of the coated layer at a radius ratio of 1.53 with a poly taper tension profile, (g) cross-sectional image of the coated layer at a radius ratio of 4.93 with a poly taper tension profile.

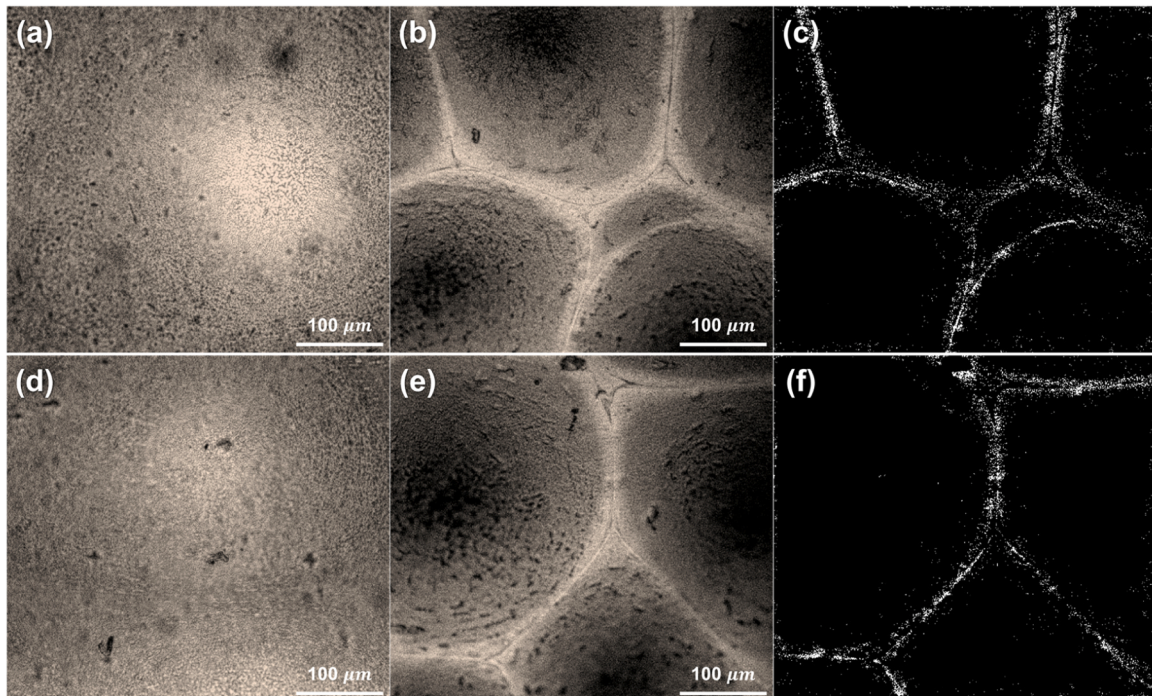


Fig. 14. Microscopic images of the surface of the coated layer with a maximum winding length of 1400 m: (a) surface image at a radius ratio of 4.93 with parabolic taper tension, (b) surface image at a radius ratio of 1.02 with a parabolic taper tension profile, (c) crack detection image at a radius ratio of 1.02 with a parabolic taper tension profile, (d) surface image at a radius ratio of 4.93 with poly taper tension, (e) surface image at a radius ratio of 1.02 with poly taper tension, (f) crack detection image at a radius ratio of 1.02 with a poly taper tension profile.

application of a parabolic taper tension profile, the radial stress was found to be minimal at the outer layer of the wound roll, leading to the absence of crack defects on the surface of the coated layer, as illustrated in Fig. 14(a). However, on the inner layer surface, significant cracks were observed due to relatively high radial stress, as depicted in Fig. 14(b). To quantitatively assess the crack area, image data was binarized, isolating only the cracked area, as observed in Fig. 14(c). Fig. 14(d) exhibits the outermost surface of the coated layer when the poly taper tension was employed. When using the poly taper tension profile, cracks are limited to a relatively small area on the coated layer surface because the radial stress reduction effect is predominantly maintained, even as the winding length increases. This image data was also binary processed

to isolate only the cracked areas, as shown in Fig. 14(f). Utilizing these processed images, the area density value was calculated, representing the proportion of the cracked area to the non-cracked area. Applying the parabolic taper tension profile resulted in an area density of 5.9 %, while the poly taper tension profile yielded an area density of 4.3 %. This corresponds to an approximate reduction in crack defects of 27.1 % when the poly taper tension profile was used.

5. Conclusion

In the roll-to-roll winding process, where a substantial amount of the web and coated layer are wound onto a central core, radial stress and

hoop stress are generated within the roll. These stresses have been identified as causes of defects on the coated layer within the wound roll. The most effective and sole method for preventing these defects is the application of a taper tension profile during the winding process. To enhance productivity, the length of the web wound on a single core has been extended, resulting in increased moment of inertia in the rewinder. This increase in moment of inertia contributes to tension errors when employing the taper tension profile. In this study, a polynomial-based taper tension profile was developed, aimed at effectively reducing radial stress and minimizing defects in the coated layer during the winding process of an electrolyte layer. The main contributions of this study are as follows.

- The poly taper tension profile reduced maximum tension error by approximately 16.1 % compared to the parabolic taper tension profile.
- This reduction in tension error preserved the radial stress reduction effect, resulting in a 13.3 % decrease in maximum radial stress.
- Utilizing the poly taper tension profile improved the variation in coated layer thickness by 33.3 % compared to the parabolic taper tension profile.
- The occurrence of crack defects on the coated layer in the innermost section of the wound roll was reduced by 27.1 %.

The application of the poly taper tension profile, especially in the case where the maximum winding length needs to be continuously increased, has proven to be effective in reducing tension errors when compared to conventional taper tension profiles, while maintaining the radial stress reduction effect. This, in turn, contributes to a more uniform quality of the coated layer as the maximum winding length progressively extends.

CRediT authorship contribution statement

Changwoo Lee: Funding acquisition, Project administration, Supervision, Validation, Writing – review & editing. **Jaehyun Noh:** Conceptualization, Data curation, Formal analysis, Investigation, Methodology, Software, Validation, Visualization, Writing – original draft. **Minjae Kim:** Data curation, Investigation, Visualization. **Minho Jo:** Data curation, Formal analysis, Software, Validation.

Declaration of Competing Interest

The authors declare that they have no known competing financial interests or personal relationships that could have appeared to influence the work reported in this paper.

Acknowledgements

This research was supported by the National Research Council of Science & Technology (NST) grant from the Korean government (MSIT) [No. CAP22082–301]; and the National Research Foundation of Korea (NRF) grant funded by the Korean government (MSIT) [No. 2020R1A5A1019649].

References

- [1] J. Kim, J. Ahn, J. Shin, K.J. Yoon, J.W. Son, J.H. Lee, D. Shin, H.W. Lee, H. Ji, Enhanced sinterability and electrochemical performance of solid oxide fuel cells via a roll calendering process, *J. Mater. Chem. A*, **III**, 7 (2019) 9958–9967, <https://doi.org/10.1039/C9TA01818B>.
- [2] C. Goebel, V. Asokan, S. Khieu, J.E. Svensson, J. Froitzheim, Self-healing properties of Ce/Co-coated stainless steel under simulated intermediate temperature solid oxide fuel cell conditions, *Surf. Coat. Technol.* **428** (2021) 127894, <https://doi.org/10.1016/j.surcoat.2021.127894>.
- [3] H. Li, C. Zuo, A.D. Scully, D. Angmo, J. Yang, M. Gao, Recent progress towards roll-to-roll manufacturing of perovskite solar cells using slot-die processing, *Flex. Print. Electron.* **5** (2020), <https://doi.org/10.1088/2058-8585/ab639e>.
- [4] Y.Y. Kim, T.Y. Yang, R. Suhonen, A. Kemppainen, K. Hwang, N.J. Jeon, J. Seo, Roll-to-roll gravure-printed flexible perovskite solar cells using eco-friendly antisolvent bathing with wide processing window, *Nat. Commun.* **11** (2020) 5146, <https://doi.org/10.1038/s41467-020-18940-5>.
- [5] K. Sato, S. Uchida, S. Toriyama, S. Nishimura, K. Oyaizu, H. Nishide, Y. Nishikitani, Low-cost, organic light-emitting electrochemical cells with mass-producible nanoimprinted substrates made using roll-to-roll methods, *Adv. Mater. Technol.* **2** (2017), <https://doi.org/10.1002/admt.201600293>.
- [6] R.R. Søndergaard, M. Hösel, F.C. Krebs, Roll-to-Roll fabrication of large area functional organic materials, *J. Polym. Sci. Part B Polym. Phys.* **51** (2013) 16–34, <https://doi.org/10.1002/polb.23192>.
- [7] H. Koo, W. Lee, Y. Choi, J. Sun, J. Bak, J. Noh, V. Subramanian, Y. Azuma, Y. Majima, G. Cho, Scalability of carbon-nanotube-based thin film transistors for flexible electronic devices manufactured using an all roll-to-roll gravure printing system, *Sci. Rep.* **5** (2015) 1–11, <https://doi.org/10.1038/srep14459>.
- [8] H. Jeong, Y. Noh, J. Kim, S. Ko, D. Lee, Sequential manufacturing via intra-additive hybrid materials approach for fully roll-to-roll processed flexible organic thin film transistors, *J. Manuf. Process.* **72** (2021) 138–147, <https://doi.org/10.1016/j.jmapro.2021.10.001>.
- [9] C.H. Chao, C.T. Hsieh, W.J. Ke, L.W. Lee, Y.F. Lin, H.W. Liu, S. Gu, C.C. Fu, R. S. Juan, B.C. Mallick, Y.A. Gandomi, C.Y. Su, Roll-to-roll atomic layer deposition of titania coating on polymeric separators for lithium ion batteries, *J. Power Sources* **482** (2021) 228896, <https://doi.org/10.1016/j.jpowsour.2020.228896>.
- [10] C. Luo, J. Wang, X. Fan, Y. Zhu, F. Han, L. Suo, C. Wang, Roll-to-roll fabrication of organic nanorod electrodes for sodium ion batteries, *Nano Energy* **13** (2015) 537–545, <https://doi.org/10.1016/j.nanoen.2015.03.041>.
- [11] Z. Chen, Y. Zheng, T. Zhang, D.S.H. Wong, Z. Deng, Modeling and register control of the speed-up phase in roll-to-roll printing systems, *IEEE Trans. Autom. Sci. Eng.* **16** (2019) 1438–1449, <https://doi.org/10.1109/TASE.2018.2881994>.
- [12] C. Zwahr, N. Serey, L. Nitschke, C. Bischoff, U. Rädel, A. Meyer, P. Zhu, W. Pfleger, Targeting new ways for large-scale, high-speed surface functionalization using direct laser interference patterning in a roll-to-roll process, *Int. J. Extrem. Manuf.* **5** (2023), <https://doi.org/10.1088/2631-7990/acd916>.
- [13] Y.S. Park, H.K. Kim, S.W. Jeong, W.J. Cho, Highly flexible indium zinc oxide electrode grown on PET substrate by cost efficient roll-to-roll sputtering process, *Thin Solid Films* **518** (2010) 3071–3074, <https://doi.org/10.1016/j.tsf.2009.09.197>.
- [14] D.J. Kim, H.I. Shin, E.H. Ko, K.H. Kim, T.W. Kim, H.K. Kim, Roll-to-roll slot-die coating of 400 mm wide, flexible, transparent Ag nanowire films for flexible touch screen panels, *Sci. Rep.* **6** (2016) 1–12, <https://doi.org/10.1038/srep34322>.
- [15] T. Syrový, T. Kazda, J. Akram, L. Syrová, Towards roll-to-roll printed batteries based on organic electrodes for printed electronics applications, *J. Energy Storage* **40** (2021), <https://doi.org/10.1016/j.est.2021.102680>.
- [16] E. Sowade, H. Kang, K.Y. Mitra, O.J. Weiß, J. Weber, R.R. Baumann, Roll-to-roll infrared (IR) drying and sintering of an inkjet-printed silver nanoparticle ink within 1 second, *J. Mater. Chem. C* **3** (2015) 11815–11826, <https://doi.org/10.1039/C5TC02291F>.
- [17] C. Koidis, S. Logothetidis, A. Ioakeimidis, A. Laskarakis, C. Kapnopoulos, Key factors to improve the efficiency of roll-to-roll printed organic photovoltaics, *Org. Electron.* **14** (2013) 1744–1748, <https://doi.org/10.1016/j.orgel.2013.04.015>.
- [18] K. Robinson, W. Durkin, Electrostatic issues in roll-to-roll manufacturing operations, *IEEE Trans. Ind. Appl.* **46** (2010) 2172–2178, <https://doi.org/10.1109/TIA.2010.2071270>.
- [19] P.R. Kidambi, D.D. Mariappan, N.T. Dee, A. Vyatskikh, S. Zhang, R. Karnik, A. J. Hart, A scalable route to nanoporous large-area atomically thin graphene membranes by roll-to-roll chemical vapor deposition and polymer support casting, *ACS Appl. Mater. Interfaces* **10** (2018) 10369–10378, <https://doi.org/10.1021/acsami.8b00846>.
- [20] N. Hong, D. Kireev, Q. Zhao, D. Chen, D. Akinwande, W. Li, Roll-to-roll dry transfer of large-scale graphene, *Adv. Mater.* **34** (2022) e2106615, <https://doi.org/10.1002/adma.202106615>.
- [21] D. Richards, D. Burkitt, R. Patidar, D. Beynon, T. Watson, Predicting a process window for the roll-to-roll deposition of solvent-engineered SnO₂ in perovskite solar cells, *Mater. Adv., Mater. Adv.* **3** (2022) 8588–8596, <https://doi.org/10.1039/D2MA00841F>.
- [22] M. Ghorab, A. Fattah, M. Joodaki, Tensile mechanical strain effects on the electrical characteristics of roll-to-roll printed OSC, *IEEE J. Photovolt.* **12** (2022) 737–743, <https://doi.org/10.1109/JPHOTOV.2022.3148717>.
- [23] P. Liu, D. Yang, B. Li, C. Zhang, P. Ming, Recent progress of catalyst ink for roll-to-roll manufacturing paired with slot die coating for proton exchange membrane fuel cells, *Int. J. Hydrog. Energy* **48** (2023) 19666–19685, <https://doi.org/10.1016/j.ijhydene.2023.02.022>.
- [24] J. Noh, M. Jo, H. Jeon, M. Kim, J. Jo, C. Lee, Web wrinkle defects due to temperature profile in roll-to-roll manufacturing systems, *Polymers* **15** (2023), <https://doi.org/10.3390/polym15020457>.
- [25] H. Jeon, J. Noh, M. Kim, M. Jo, S.H. Nam, J. Jo, C. Lee, Control methodology for tensioned web considering thermal behavior in roll-to-roll manufacturing systems, *Eng. Sci. Technol. Int. J.* **46** (2023) 101508, <https://doi.org/10.1016/j.jestch.2023.101508>.
- [26] H. Jeong, Y. Noh, G.Y. Kim, H. Lee, D. Lee, Roll-to-roll processed silver nanowire/silicon dioxide microsphere composite for high-accuracy flexible touch sensing application, *Surf. Interfaces* **30** (2022) 101976, <https://doi.org/10.1016/j.surfin.2022.101976>.
- [27] P.S. Chandrasekhar, S. Chapagain, M. Blake, P.J. Armstrong, C. Grapperhaus, T. L. Druffel, Rapid scalable fabrication of roll-to-roll slot-die coated flexible

- perovskite solar cells using intense pulse light annealing, *Sustain. Energy Fuels.* 6 (2022) 5316–5323, <https://doi.org/10.1039/D2SE00911K>.
- [28] M. Yamada, N. Soma, M. Tsuta, S. Nakamura, N. Ando, F. Matsumoto, Development of a roll-to-roll high-speed laser micro processing machine for preparing through-holed anodes and cathodes of lithium-ion batteries, *Int. J. Extrem. Manuf.* 5 (2023), <https://doi.org/10.1088/2631-7990/acd917>.
- [29] M.L. Liu, A nonlinear model of center-wound rolls incorporating refined boundary conditions, *Comput. Struct.* 87 (2009) 552–563, <https://doi.org/10.1016/j.compstruc.2009.02.008>.
- [30] K. Acton, B. Weick, Orthotropic viscoelastic behavior of polymer tape in a wound roll, *Mech. Adv. Mater. Struct.* 21 (2014) 53–66, <https://doi.org/10.1080/15376494.2012.677106>.
- [31] C. Mollamahmutoglu, J.K. Good, Modeling the influence of web thickness and length imperfections resulting from manufacturing processes on wound roll stresses, *CIRP J. Manuf. Sci. Technol.* 8 (2015) 22–33, <https://doi.org/10.1016/j.cirpj.2014.10.004>.
- [32] R. Li, W. Li, A. Singh, D. Ren, Z. Hou, M. Ouyang, Effect of external pressure and internal stress on battery performance and lifespan, *Energy Storage Mater.* 52 (2022) 395–429, <https://doi.org/10.1016/j.ensm.2022.07.034>.
- [33] J. Noh, M. Jo, G. Cho, S. Nam, C. Lee, Effect of radial stress on the nanoparticle-based electrolyte layer in a center-wound roll with roll-to-roll systems, *Nanomater.* (Basel). 12 (2022), <https://doi.org/10.3390/nano12061014>.
- [34] H.C. Altmann, Formulas for computing the stresses in center-wound rolls, *Tappi J.* 51 (1968) 176.
- [35] H.P. Yagoda, Resolution of a core problem in wound rolls, *J. Appl. Mech.* 47 (1980) 847–854, <https://doi.org/10.1115/1.3153801>.
- [36] Z. Hakiel, Nonlinear model for wound roll stress, *Tappi J.* 70 (1987) 113–117.
- [37] C. Mollamahmutoglu, J.K. Good, Analysis of large deformation wound roll models, *J. Appl. Mech.* 80 (2013) 041016, <https://doi.org/10.1115/1.4023034>.
- [38] S.J. Burns, R.R. Meehan, J.C. Lambopoulos, Strain-based formulas for stresses in profiled center-wound rolls, *Tappi J.* 82 (1999).
- [39] J. Lee, C. Lee, Model-based winding tension profile to minimize radial stress in a flexible substrate in a roll-to-roll web transporting system, *IEEE ASME Trans. Mechatron.* 23 (2018) 2928–2939, <https://doi.org/10.1109/TMECH.2018.2873244>.
- [40] D. Wu, S. Lin, Advanced winding tension method for preventing axial slip of the center-wound roll, *Precis. Eng.* 84 (2023) 102–109, <https://doi.org/10.1016/j.precisioneng.2023.08.001>.
- [41] Z. Chen, Y. Zheng, T. Zhang, D.S.H. Wong, Z. Deng, Modeling and register control of the Speed-up phase in roll-to-roll printing systems, *IEEE Trans. Autom. Sci. Eng.* 16 (2019) 1438–1449, <https://doi.org/10.1109/TASE.2018.2881994>.
- [42] J. Seong, J. Park, J. Lee, B. Ahn, J.H. Yeom, J. Kim, T. Hassinen, S. Rhee, S. Ko, D. Lee, K.H. Shin, Practical design guidelines for the development of high-precision roll-to-roll slot-die coating equipment and the process, *IEEE Trans. Compon. Packag. Manuf. Technol.* 6 (2016) 1677–1686, <https://doi.org/10.1109/TCMT.2016.2613141>.
- [43] P.R. Raul, S.G. Manyam, P.R. Pagilla, S. Darbha, Output regulation of nonlinear systems with application to roll-to-roll manufacturing systems, *IEEE ASME Trans. Mechatron.* 20 (2015) 1089–1098, <https://doi.org/10.1109/TMECH.2014.2366033>.
- [44] T. Xia, Y. Li, J. Li, L. Li, X. Chen, Stress distribution of the nonwoven fabric package during winding, *Text. Res. J.* 93 (2023) 2191–2201, <https://doi.org/10.1177/00405175221142246>.
- [45] Z. Chen, B. Qu, B. Jiang, S.R. Forrest, J. Ni, Robust constrained tension control for high-precision roll-to-roll processes, *ISA Trans.* 136 (2023) 651–662, <https://doi.org/10.1016/j.isatra.2022.11.020>.
- [46] P.R. Raul, P.R. Pagilla, Design and implementation of adaptive PI control schemes for web tension control in roll-to-roll (R2R) manufacturing, *ISA Trans.* 56 (2015) 276–287, <https://doi.org/10.1016/j.isatra.2014.11.020>.
- [47] S. Tsai, S.C. Mukhopadhyay, N. Yoksen, J.Y. Chang, Design of lateral dynamics control for web Roll-to-Roll systems. 2012 19th Int. Conf. Mechatron. Mach. Vis. Pract., M2VIP (2012) 339–343.
- [48] H. Kang, K.H. Shin, Precise tension control of a dancer with a reduced-order observer for roll-to-roll manufacturing systems, *Mech. Mach. Theor.* 122 (2018) 75–85, <https://doi.org/10.1016/j.mechmachtheory.2017.12.012>.
- [49] H. Shui, X. Jin, J. Ni, Twofold variation propagation modeling and analysis for roll-to-roll manufacturing systems, *IEEE Trans. Autom. Sci. Eng.* 16 (2019) 599–612, <https://doi.org/10.1109/TASE.2018.2844168>.
- [50] Z. Liang, L. Wang, B. Xue, R. Ji, D. Du, B. Chang, Sag feedback based multi-roll coordinating optimal control of a low-tension roll-to-roll system, *J. Manuf. Syst.* 61 (2021) 351–364, <https://doi.org/10.1016/j.jmsy.2021.09.016>.
- [51] W.E. Hawkins, *The plastic film and foil web handling guide*, CRC press, 2002, pp. 17–19.
- [52] J. Lee, J. Byeon, C. Lee, Fabrication of thickness-controllable double layer electrolyte using roll-to-roll additive manufacturing system, *Int. J. Precis. Eng. Manuf. - Green. Technol.* 7 (2020) 635–642, <https://doi.org/10.1007/s40684-020-00200-y>.